



# An energy-saving photo-rechargeable lithium-ion battery based on lead-free hybrid perovskite

Xiaojing Yin<sup>1</sup>, Guangran Di<sup>1</sup>, Ye Liu<sup>1</sup>, Guoqiang Wang<sup>1</sup>, Changhua Mi<sup>1</sup>, Yubo Kuang<sup>1</sup>, Xiaoqian Xiang<sup>1</sup>, Xin Sun<sup>1</sup>, Eran Edri<sup>2</sup>, Xiaojun Lv<sup>1\*</sup> and Meicheng Li<sup>1\*</sup>

**ABSTRACT** The development and utilization of clean energy have emerged as indispensable technologies within contemporary societal structures, and the development of photo-rechargeable lithium-ion batteries (PR-LIB) holds new promise for simultaneously eliminating solar energy volatility limitations and realizing battery self-charging. In this study, we present photoactive electrodes consisting of lead-free bismuth-based hybrid perovskite that combine the dual functions of photovoltaic conversion and energy storage. It was found that the PR-LIB based on this electrode increased the discharge capacity of the battery from 236.0 mA h g<sup>-1</sup> in the dark to 282.4 mA h g<sup>-1</sup> (a current density of 50 mA g<sup>-1</sup>) with a growth rate of 19.7% under light conditions. The photo-generated carriers generated by the methylammonium bismuth iodide (MBI) effectively accelerated the charge transfer and lithium-ion diffusion, which contributed to the increase of the capacity and the decrease of the charge-transfer resistance. Furthermore, the charging potential decreased by 0.1 V (6% reduction in input power) while the discharging potential increased by 0.1 V (11.8% increase in output power) under light. This work demonstrates the potential of PR-LIB as an efficient, energy-saving battery in portable electronic devices.

**Keywords:** lithium-ion batteries, photo-rechargeable batteries, hybrid perovskite, photoactive electrodes, energy conservation

## INTRODUCTION

Faced with the serious challenges of global climate change and increasing energy shortages, energy conservation has become the focus of our common concern [1,2]. Integrated photovoltaic storage devices, which combine photovoltaic conversion units and energy storage units, can reduce carbon emissions and improve energy utilization, making them a promising technology in the field of energy conservation [3]. In the integrated photovoltaic storage device, compared with the three-electrode system in which charge generation and charge storage take place in a separate space, the two-electrode system is composed of materials with the two functions of charge generation and charge storage in a single electrode to form a photoelectrode (PE) [4–6]. The two-electrode system is characterized by its simple structure, miniaturization, and lightweight, while the development of

bifunctional materials has great potential in the field of sustainable development in the future. Among the two-electrode systems, photo-rechargeable lithium-ion batteries (PR-LIB) have been widely studied for their high energy storage capacity [7–9]. They can directly convert solar energy into electrical energy and store it in the form of chemical energy, and additional photo-generated carriers can alleviate the problems of charging overpotential and slow charging rate [10,11]. PE is the most important component in PR-LIBs, and candidates for photo-electrodes must have certain conditions such as a suitable bandgap, a sufficient number of active sites, and channels for ion transport [12].

Numerous inorganic [13–17], organic [18], and inorganic-organic hybrid combinations [19–21] have been explored for PE that exhibit dual-energy storage and conversion capabilities. Single-component photo-electrochemical storage materials are classified into three distinctive categories. (1) Inorganic metal oxides: Possessing a distinct and varied structure, they harness solar energy via their photovoltaic property and redox-active lattice. Representative examples include V<sub>2</sub>O<sub>5</sub> [22] and TiO<sub>2</sub> [23–25], which are the most extensively utilized bifunctional materials. (2) Organic small molecules featuring redox sites: Organic molecules have the advantages of low cost and design flexibility over conventional inorganic metal oxide-based materials. This is because they can be constructed from a variety of building blocks, allowing fine-tuning of visible light sensitivity, band gaps and band edges. For instance, organic materials incorporating tunable redox functional groups (such as C=O) exhibit stable and reversible Li<sup>+</sup> coordination [26]. (3) Organic-inorganic hybrid materials: their superior optoelectronic attributes, encompassing adjustable energy band gaps, extensive charge transport distances, and elevated absorption coefficients, have garnered interest as bifunctional materials [27]. The electron-hole pairs generated by single-component photoelectrochemical storage materials often face difficulties in efficient separation, with their energies frequently dissipated by carrier complexation processes. Consequently, numerous research endeavors have assembled multicomponent photoelectrochemical storage materials layer by layer for enhanced charge separation. TiO<sub>2</sub> is conveniently modifiable and combines seamlessly with other materials to form photoelectrodes. TiO<sub>2</sub> functions as a photoactive layer to generate electron-hole pairs

<sup>1</sup> State Key Laboratory of Alternate Electrical Power System with Renewable Energy Sources, School of New Energy, North China Electric Power University, Beijing 102206, China

<sup>2</sup> IlseKatz Institute for Nanoscale Science and Technology, Department of Chemical Engineering, Ben-Gurion University of the Negev, Be'er-Sheva 8410501, Israel

\* Corresponding author (email: lvxiaojun@ncepu.edu.cn; mcli@ncepu.edu.cn)

upon exposure to light.  $V_2O_5$  [28],  $SnO_2$  [29], and  $Cu_2O$  [30], which possess energetically compatible levels with respect to the photoactive layer, serve as photoelectric transport and energy storage layers, respectively, ensuring efficient interfacial electron-hole transfer from  $TiO_2$ . Furthermore, Boruah *et al.* [31] incorporated  $V_2O_5$  nanofibers with P3HT and reduced graphene oxide (rGO) for solar energy conversion and lithium-ion storage. Upon illumination, photoexcited electrons from  $V_2O_5$  nanofibers were transferred to P3HT and subsequently traversed rGO ( $-4.4$  eV) to reach the collector due to the matched energy levels between  $V_2O_5$  ( $-2.4$  eV) and P3HT ( $-3.2$  eV). These multicomponent photoelectrochemical storage materials demonstrated efficacy in augmenting the carrier density and enhancing the photoelectric conversion efficiency of PR-LIB.

Hybrid perovskites, well-known for their distinctive crystal structure and exceptional photovoltaic properties, are used in solar cells [32–34], light-emitting diodes [35,36], and lasers [37,38], among other applications. In addition to their unique electronic and photonic characteristics, the observed ion mobility diffusion was initially perceived as a detrimental factor in perovskite solar cells, often resulting in suboptimal and unstable overall conversion efficiencies [39,40]. Fortunately, this property broadens their utility in lithium-ion batteries [41–43]. Hybrid perovskites have demonstrated lithium-ion ( $Li^+$ ) diffusion coefficients as high as  $10^{-7}$   $cm^2 s^{-1}$ , rendering them rapid ionic conductors [44]. Xia *et al.* simulated the probable sites for lithium-ion intercalation into lead-based hybrid perovskites ( $CH_3NH_3PbBr_3$ ) and verified the occurrence of intercalation (lithiation) and conversion reactions during charge/discharge cycles experimentally [45]. Hybrid perovskites possess a dual functionality of photovoltaic conversion and storage, thus making them ideal for use as a PE in PR-LIB [46]. Ahmad's team chose lead-based hybrid perovskite ( $(C_6H_9C_2H_4NH_3)_2PbI_4$ ) as the PE material, and the cell achieved photo-charging over a limited voltage range and without external bias [21]. Since the photoelectric conversion efficiency of this work is only 0.034% and the avoidance of the light-assisted discharge process, a study has been carried out to achieve an integrated light-assisted lithium-ion battery with DAPBI as the cathode, where energy saving is achieved by increasing the discharge voltage and decreasing the charging voltage under light [27]. PR-LIBs currently suffer from low solar energy utilization, low photoelectrochemical energy storage efficiency and poor stability [47], which greatly hinder the industrialization and commercialization value of such batteries.

Herein, we are the first to construct a photo-rechargeable lithium-ion battery based on a non-toxic and air-stable bismuth-based hybrid perovskite as a photoactive electrode, which possesses the dual functions of photoelectric conversion and energy storage. Under solar illumination, the integrated device's charging potential was reduced by 0.1 V and the input power by 6%, in addition to the increase in charging capacity. The light-assisted discharge achieved a 19.7% increase in discharge capacity (current density 50 mA  $g^{-1}$ ), along with a 0.1 V increase in discharge potential and an 11.8% increase in output power. The photoelectrode achieves effective charge separation during charge/discharge under light, and the photogenerated carriers accelerate the transport/diffusion of lithium-ion in the electrode and promote electrochemical reaction kinetics. The construction of the system successfully achieves a reduction in power consumption and energy saving, and the mechanism of electron

generation, transfer and storage in the system has great potential to bring new technologies for miniaturized and lightweight battery applications.

## EXPERIMENTAL

### Materials

The chemicals were purchased from the following companies. bismuth iodide ( $BiI_3$ ) (99.99%, Aladdin), methylammonium iodide ( $CH_3NH_3I$ ) (99.5%, Yuri Solar CO., Ltd., China), dimethyl sulfoxide (DMSO) (99.9%, Alfa), *N,N*-dimethylformamide (DMF) (99.5%, Aladdin), *N*-methylpyrrolidone (NMP) (99.9%, Aladdin), polyvinylidene fluoride (PVDF) (Macklin), 1 M lithium hexafluorophosphate ( $LiPF_6$ ) in ethylene carbonate (EC), diethyl carbonate (DEC), dimethyl carbonate (DMC) (1:1:1 in volume) (DoDoChem), Li metal foil (DoDoChem).

### Synthesis of $(CH_3NH_3)_3Bi_2I_9$ (MBI)

Methylammonium bismuth iodide (MBI) is commonly produced by dissolving  $BiI_3$  (1.65 M) and  $CH_3NH_3I$  (2.475 M) in a mixture of DMSO and DMF in a 1:1 ratio by volume. The solution is then stirred at 60°C for 5 h, and the resulting perovskite powder is obtained by drying the solution under vacuum at 120°C.

### Preparation of electrodes

To prepare the electrodes, rGO is dissolved in 1 mL of NMP through sonication, which is continued for 2 h. Next, perovskite powder is added to the solution and stirred for 12 h. Subsequently, PVDF is mixed and stirred for 12 h. Finally, 60  $\mu$ L of the resulting solution is drop-casted onto the pre-cleaned indium tin oxide (ITO) substrate and left to dry at 120°C overnight.

### Material characterization

The crystal structures were analyzed with an X-ray diffractometer (XRD) (Smart Lab SE, Rigaku). The optical properties were characterized with a UV-Vis spectrophotometer (UV-2600i, Shimadzu Corporation). The samples were analyzed for their morphology and elemental composition with a scanning electron microscope (SEM) (TM4000Plus, Hitachi Limited). Additionally, the composition and chemical state of the material were studied by X-ray photoelectron spectroscopy (XPS) (ESCALAB 250Xi, Thermo Scientific).

### Preparation of photo-rechargeable lithium-ion battery (PR-LIB)

A homemade battery case with a hole (8 mm in diameter) in the positive shell was used to make a coin cell that allows light transmission. The hole was sealed with ITO glass and epoxy resin to ensure airtightness. The photoactive electrode was then placed and connected to the button cell using carbon conductive tape for electrical connection. The battery housing was transferred to the glove box, where a Whatman glass microfiber filter paper separator impregnated with  $LiPF_6$  and lithium metal foil was assembled. Finally, Li counter electrodes were placed and assembled into PR-LIB according to standard procedures.

### Electrochemical measurements

A 300 W xenon lamp is used to simulate the intensity of sunlight. The charge/discharge test under light and dark conditions was performed on the Land-CT3002A multi-channel battery test system in the voltage range of 0.1–2.5 V and 0.8–2.5 V. The

cyclic voltammetry (CV) test (voltage range 0.1–2.5 V and 0.8–2.5 V) at different scan rates, chronoamperometry, and the electrochemical impedance spectroscopy (EIS) test were performed on a CHI Electrochemical Analyzer (CHI660E).

## RESULTS AND DISCUSSION

The structures of the powder specimens were examined meticulously through X-ray diffraction (XRD) graphic analysis. Refer to Fig. 1a which demonstrates experimental findings in harmony with prior studies regarding the crystal architecture of methylammonium bismuth iodide ( $(\text{CH}_3\text{NH}_3)_3\text{Bi}_2\text{I}_9$ , hereafter referred to as MBI) [48–50]. Notably, MBI falls under the hexagonally assembled lattice system (designated as  $P6_3/mmc$ ). In addition, MBI exhibits excellent stability for 30 days when continuously exposed to humidity and ambient air at room temperature. The MBI in the electrodes showed a hexagonal morphology (width range 40–60  $\mu\text{m}$ ) (Fig. 1b), and these hexagons consisted of small hexagonal lamellae (Fig. 1c). Fig. 1d underscores the superior absorbance characteristics of MBI. The spectral absorption profile, recorded across 300–800 nm, illuminates that the material exhibits an optical band gap of 1.83 eV, as indicated in the inset of Fig. 1d. According to the ultraviolet photoelectron

spectroscopy (UPS) analysis (Fig. 1e), a work function of the material (5.21 eV), signifying the disparity between the Fermi energy level  $E_F$  and the vacuum energy level, is deduced from the spectra high binding energy cut-offs [51], whereas the material ionization potential (6.19 eV) is calculated by adding the photoemission onset of the valence-side  $E_{VB}$  to the Fermi energy level  $E_F$  (0.98 eV). To attain a more profound comprehension of the elemental constitution and valence attributes of MBI, thereby facilitating a more precise analysis of the operating mechanism of PR-LIB, X-ray photoelectron spectroscopy (XPS) analyses were performed on this substance. From the measured spectra of MBI, the elements identified encompassed Bi, I, N, and C (Fig. S1). The two distinctive peaks at 164.1 and 158.8 eV in Fig. 1f are assigned to Bi  $4f_{5/2}$  and Bi  $4f_{7/2}$ , respectively, representing the signature signal peaks of  $\text{Bi}^{3+}$  [52,53]. According to the reported literature [54], two small peaks may be related to zero-valent metal bismuth, which is suggested to be induced in part during the measurement of the XPS spectra. The peaks at I  $3d_{5/2}$  (618.8 eV) and I  $3d_{3/2}$  (630.6 eV) in Fig. 1g are ascribed to the characteristic signatures of  $\text{I}^-$  compounds.

The PR-LIB's PE is fabricated using a blend of MBI, rGO, and PVDF in an optimal proportion of 8:1:1 respectively. rGO serves

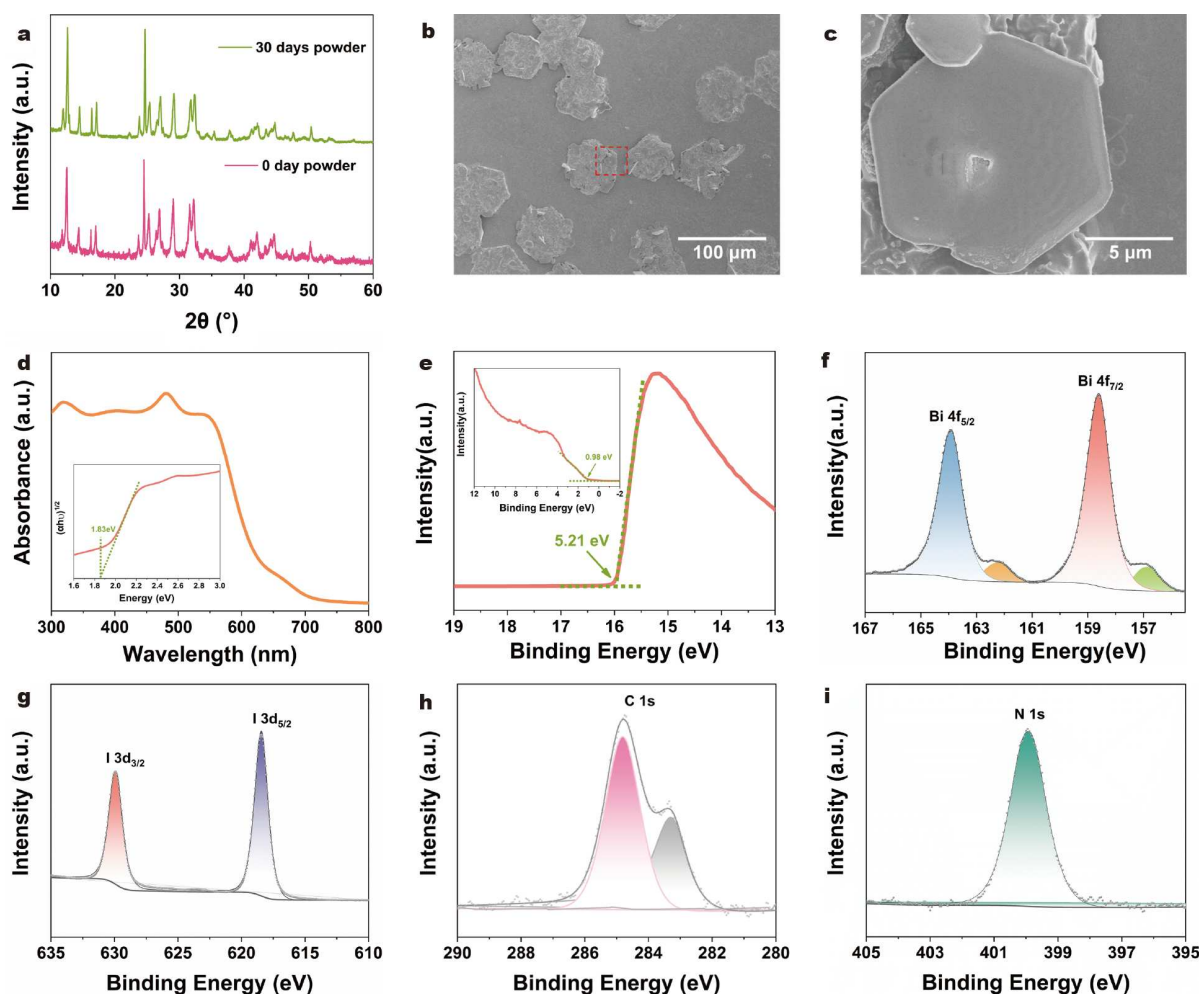


**Figure 1** (a) XRD patterns of powder MBI exposed to air at different time points. (b) SEM image of the surface morphologies of MBI (The scale bar is 100  $\mu\text{m}$ ). (c) SEM image of the surface morphologies of MBI (The scale bar is 5  $\mu\text{m}$ ). (d) Absorption spectra of MBI. Inset: Tauc plot of MBI. (e) UPS spectra showing the valence region of MBI on gold foil and the secondary-electron cutoff used to determine the work function of the sample. XPS spectra of MBI: (f) Bi 4f, (g) I 3d, (h) C 1s, and (i) N 1s.

as a semiconductive enhancing agent and a selective electron transport layer due to its exceptional bandgap compatibility with MBI. This facilitates the transfer of photoexcited electrons from the active layer to rGO and subsequently to the counter electrode through an external electrical pathway. On the other hand, PVDF functions as a binding agent, ensuring the cohesion between the electrode components and their adherence to the collector. The detailed assembly procedure of the PR-LIB is illustrated in Fig. S2 of the supplementary information. The PE is fabricated within a voltage range of 0.1–2.5 V. Cyclic voltammetry evaluations were performed on the cells at a scan rate of  $0.5 \text{ mV s}^{-1}$  (Fig. 2a). The comparison of the CV cycle curves shows the changes in the internal chemical reactions of the PR-LIB. The reduction peaks observed in the low voltage domain are primarily attributed to processes like solid electrolyte interface (SEI) formation and bismuth alloying/dealloying [55], which may lead to structural changes in MBI. In the subsequent second cycle, the changes in peak position and intensity explain the gradual decrease in cycle efficiency in the 0.1–2.5 V cycle. As depicted in Fig. 2b, the initial discharge capacity of the battery is  $748.4 \text{ mA h g}^{-1}$ . It can be observed that although the charging curve overlap is good, the discharge curve overlap is low, indicating that the discharge reaction is not consistent during each cycle. In line with these observations, we confined the charging and discharging voltages to a minimum of 0.8 V under light exposure conditions. Fig. 2c depicts the galvanostatic charge-discharge (GCD) profile of MBI at a current density of  $50\text{--}200 \text{ mA g}^{-1}$ . With an augmentation in current density, the total amount of  $\text{Li}^+$  insertion into the electrode material gradually decreases. This could be attributed to the constrained kinetics of  $\text{Li}^+$  insertion at elevated current densities. Fig. S3 illustrates the charging and discharging at a

steady current for 100 cycles at  $50 \text{ mA g}^{-1}$  current density.

To investigate the electrochemical kinetics within the cell, cyclic voltammetry assessments were conducted at scan rates ranging from 1 to  $5 \text{ mV s}^{-1}$  (Fig. 2d). The CV profiles were recorded under darkened environments. Oxidation and reduction peaks were detected at 1.95 and 1.31 V, corresponding to the  $\text{Li}/\text{Li}^+$  transformation. The slight shift in redox potential at escalating scan speeds signifies rapid  $\text{Li}^+/\text{e}^-$  transport kinetics and reversibility of the redox reaction. The area under the CV curve includes both Faraday and non-Faraday processes, and fitting equations to analyze the charge storage mechanism can assess the corresponding charge storage kinetics. [56]. A correlation analysis may be executed based on the power law relation between the peak current ( $i$ ) and the scan rate ( $\nu$ ). When the value of  $b$  approximates 1, the system undergoes a capacitance-regulated interfacial  $\text{Li}^+$  storage process. Conversely, when the value of  $b$  nears 0.5, a diffusion-regulated  $\text{Li}^+$  embedding reaction predominantly controlled by diffusion ensues [25,57]. In the inset of Fig. 2d, peak 1 and peak 2 exhibit  $b$ -values of 0.92 and 0.79, respectively. These figures were derived by examining the correlation between the currents of the two distinct redox peaks and their corresponding scanning rates. This correlation denotes the propensity for pseudo-capacitance regulation in the cell. The quantified pseudo-capacitance control effect ( $k_1\nu$ ) and diffusion control effect ( $k_2\nu^{1/2}$ ) were subsequently computed. Fig. 2e, f depict the calculated proportions of diffusion control effects in total charge storage. The fraction of diffusion control effect diminishes from 22.29% to 11.87% as the scan rate increases from 1 to  $5 \text{ mV s}^{-1}$ . These findings suggest that the  $\text{Li}^+$  insertion process is more protracted at elevated scan rates and that capacitor-like mechanisms contribute the majority to the overall capacity.

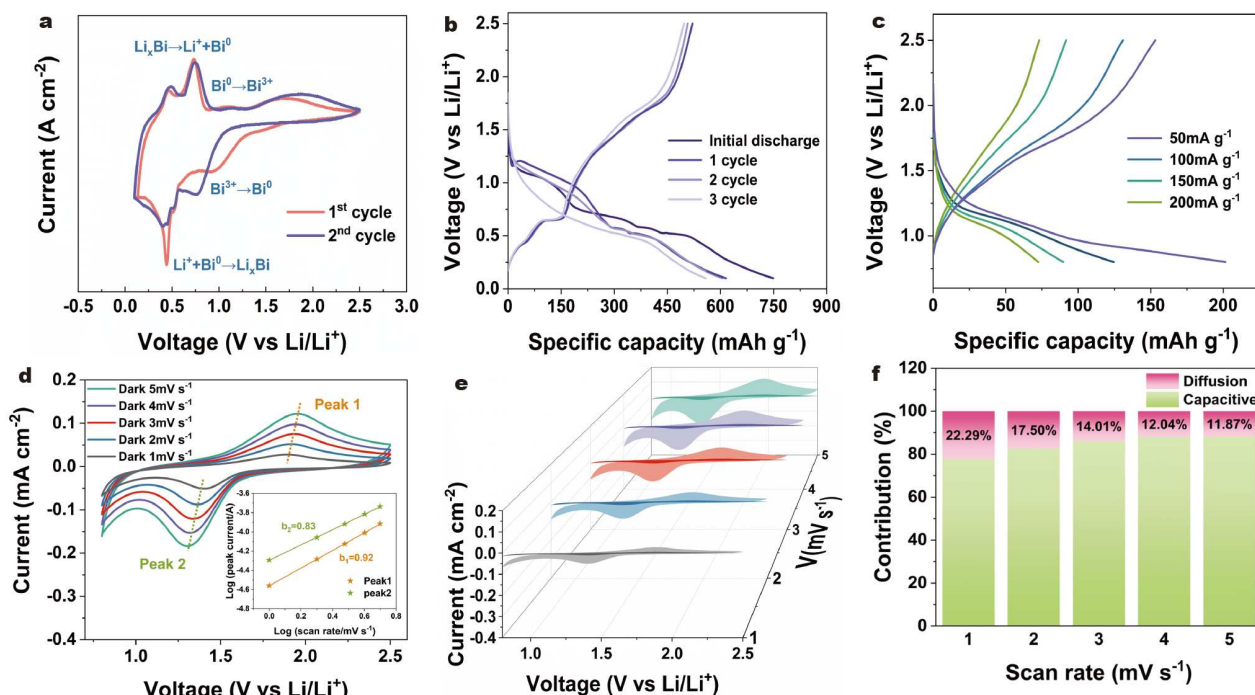


**Figure 2** Electrochemical performances of PR-LIB in the dark. (a) CV curves at  $0.5 \text{ mV s}^{-1}$  scan rate in the voltage range 0.1–2.5 V. (b) GCD curves at  $50 \text{ mA g}^{-1}$  current density in the voltage range of 0.1–2.5 V. (c) GCD curves of PE ( $50\text{--}200 \text{ mA g}^{-1}$ ). (d) CV curves at different scan rates ( $1\text{--}5 \text{ mV s}^{-1}$ ). Inset: diffusion constant analysis. (e) Three-dimensional schematic of diffusion and pseudo-capacitive processes, with diffusion control in the deep region. (f) The calculated proportion of the pseudo-capacitance and diffusion process.

To elucidate the lithium storage mechanism used by MBI materials, a series of *ex-situ* XRD examinations were conducted on these compounds at various stages within the discharge cycle. Fig. 3a depicts the XRD patterns of the electrodes of a standard coin cell battery using MBI when first discharged to different voltages. The red line in the figure shows the XRD of the initial state of the MBI after the preparation of the electrode slurry. The prominent peaks positioned at  $43.3^\circ$  and  $50.4^\circ$  correspond to the (111) and (200) crystalline planes of the copper foil containing MBI material, respectively. Notably, the characteristic planar peak (0012) of MBI shifts from its original position of ( $2\theta = 50.14^\circ$ ) towards a reduced diffraction angle ( $2\theta = 49.07^\circ$ ) as the discharge reaction unfolds (Fig. 3b). This observation indicates that the lattice accommodates  $\text{Li}^+$  embedded within the MBI, thereby increasing the  $d$ -spacing between the intercalated metal halide atoms. This further suggests that the energy storage of MBI is not triggered via a surface reaction, but rather a process intrinsic to the bulk of the material. The diffraction peak of the MBI remains largely unaltered upon discharging to 1.6 V. Upon reaching 1 and 0.8 V, distinctive peaks of  $\text{Bi}^0$  emerge at  $2\theta = 27.2^\circ$ ,  $38^\circ$ , and  $39.6^\circ$  (designated by the purple diamond pattern), indicating the transformation of  $\text{Bi}^{3+}$  into  $\text{Bi}^0$  within the lower voltage domain. Drawing upon the aforementioned findings and related literature [58,59], we propose that energy is stored in MBI through a synergistic interplay of lithiation and conversion mechanisms.

Investigations into light-induced effects on the properties of a 300 W xenon lamp simulating solar radiation were performed. The PR-LIB was cycled at various current densities under an applied potential of 0 volts (Fig. 4a). At a current density of  $50 \text{ mA g}^{-1}$ , the discharge capacity during light illumination augmented from  $236 \text{ mA h g}^{-1}$  in darkness to  $282.4 \text{ mA h g}^{-1}$ , signifying a growth rate of 19.7%. Upon light stimulation, the discharge duration was prolonged by 33 min, and a substantial enhancement in capacity was noted at  $100 \text{ mA g}^{-1}$  with a growth rate of 12.3%. To mitigate the impact of temperature on the battery [60], the PR-LIB was subjected to charging and discharging at a consistent current density of  $50 \text{ mA h g}^{-1}$  across a temperature spectrum of  $30\text{--}45^\circ\text{C}$  (Fig. 4b). As temperature rises, PR-LIB capacity progressively enhances. In the darkness, the discharge capacity is  $205.1 \text{ mA h g}^{-1}$  at  $23^\circ\text{C}$  and  $215 \text{ mA h g}^{-1}$  at  $30^\circ\text{C}$ . The calculation reveals that the capacity increment at  $30^\circ\text{C}$  is 4.83%. The core temperature after pro-

longed illumination has been confirmed as  $30.3^\circ\text{C}$  (Fig. 4b inset). To ensure that the capacity augmentation under illumination is not exclusively attributed to thermal effect, we carried out GCD experiments under monochromatic light (450 nm) without heat (Fig. S4). The capacity growth rate is 23%. The findings reveal that the electrons and holes generated and separated in the photoelectrode will accrue a certain amount of battery capacity over time. Hence, the increase in illumination intensity is significant, and this enhancement is not solely due to thermal effects. Charge carriers generated in light stimulate  $\text{Li}^+$  translocation within batteries, leading to higher battery capacity.

Furthermore, the beneficial impact of light radiation was corroborated by the instantaneous photocurrent response curve (Fig. 4c), demonstrating an appreciable increase in current upon light exposure, indicating efficient charge carrier separation. Concurrently, we acquired cyclic voltammetry data for PR-LIB under illumination at a scan rate of  $1\text{--}5 \text{ mV s}^{-1}$  (Fig. 4d) to scrutinize the quantitative contribution of pseudo-capacitance and migration to the aggregate capacitance during light activation. Notably, the estimated contribution of the diffusion mechanism is substantially elevated under continual and consistent light as opposed to darkness (Fig. 4e and Fig. S5), implying that light propels electron migration and expedites the  $\text{Li}^+$  diffusion process within the PE, thereby augmenting the capacitance. In Fig. 4f, an explicit evaluation of the CV plots under illumination and non-illumination conditions at a scan rate of  $5 \text{ mV s}^{-1}$ , clearly illustrates the considerable improvement in electrochemical performance due to luminous irradiation. Detailed comparative CV graphs for scan rates ranging from 1 to  $4 \text{ mV s}^{-1}$  can be found in Fig. S5. Besides the augmentation in current density under light exposure, the negative shift of the oxidation peaks and the positive shift of the reduction peaks signify the amplification of redox reactions within PR-LIB and the potential feasibility of harnessing solar power under illumination.

To explore the impact of illumination on the performance of the battery, a light stimulation protocol was integrated into the conventional charging and discharging procedures of the PR-LIB, and a subsequent shift in the curve's profile was monitored. Fig. 5a signifies that the introduction of light while charging triggers an abundance of charge carriers emanating from the PE, thereby inducing a substantial alteration in voltage. In the context of photo-charging, photochemically produced electrons

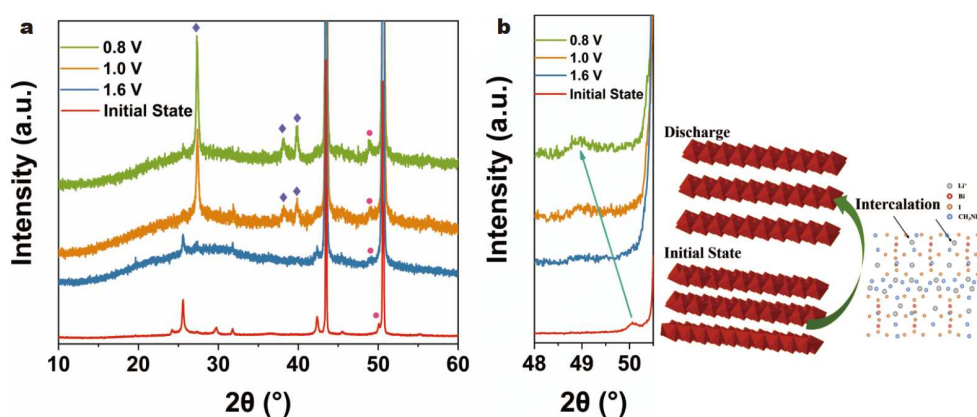


**Figure 3** (a) XRD patterns of the PE at different voltages during the first discharge process. (b) Close-up view of characteristic peak (0012) of MBI, showing a shift toward lower diffraction angle upon lithiation and layered crystal structure of MBI illustrating the increase in  $d$ -spacing upon  $\text{Li}^+$  intercalation between  $\text{Bi}_6$  octahedra.

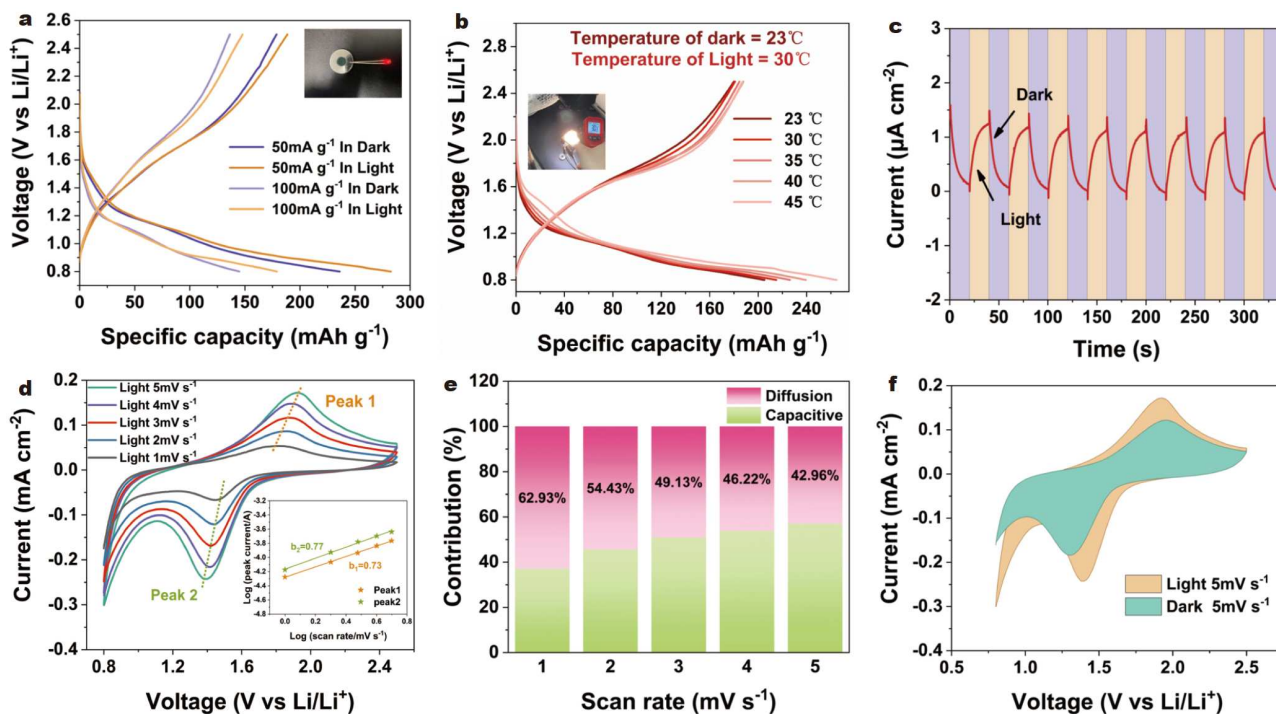


**Figure 4** Electrochemical performance of PR-LIB under illumination. (a) Capacity variation of the PE at 50 and 100 mA g<sup>-1</sup> under dark and light states. (b) Galvanostatic current discharge capacity curves of PE (23, 30, 35, 40 and 45°C). (c) *I*-*T* curves with alternating light and dark states. (d) CV curves at different scan rates (1–5 mV s<sup>-1</sup>). Inset: diffusion constant analysis. (e) The calculated proportion of the pseudo-capacitance and diffusion process. (f) CV comparisons in light and dark conditions at 5 mV s<sup>-1</sup>.

channel via the external circuit onto the Li metallic counter electrode, stimulating the reduction reaction of Li<sup>+</sup>. This phenomenon translates into a larger amount of Li<sup>+</sup> being encapsulated within the Li foil, yielding a heightened charging capacity. The photogenerated holes induce electron deficiency in the PE, incentivizing the liberation of Li<sup>+</sup> from the MBI [61]. Concurrently, upon abrupt irradiation of the PR-LIB incorporating MBI during discharge, a considerable quantity of charge carriers is engendered at the photoelectrode, resulting in a rapid change in voltage (Fig. 5b). The voltage during photo-assisted charging is diminished, whereas, during photo-assisted discharging, it surpasses conventional batteries with identical specific capacity. This observation implies that a greater quantity of Li<sup>+</sup> can be liberated/retained from the PE of the PR-LIB when the LIB and PR-LIB are charged/discharged to the same voltage. From an energy conservation standpoint, the influence of light on the operational voltage of the battery across varying current densities was scrutinized. Constant potential charging/discharging cycles were also used to demonstrate the presence of photocurrent further (Fig. S7). The currents for charging and discharging the tested cells decayed more slowly in the presence of light than in dark conditions.

As shown in Fig. 5c, we observe the charging voltage for the PR-LIB experiencing a dramatic increase from its nominal operational voltage of 1.6 V (corresponding to 25 mA g<sup>-1</sup>) to a peak value of 2.06 V (800 mA g<sup>-1</sup>) in complete darkness. Conversely, under illumination conditions, the terminal voltage reached 1.96 V, marking a decrease of 0.1 V compared to the dark condition. Correspondingly, under dark and light conditions of 800 mA g<sup>-1</sup>, the input powers of the PR-LIB were calculated as 0.33 and 0.31 mW cm<sup>-2</sup> (Fig. 5d), signifying a 6%

decline in input power, and the photoelectric conversion efficiency is 0.02%. Under illumination during discharge, the discharging voltage of the cell at each current density exceeded that observed in darkness (Fig. 5e), demonstrating a voltage discrepancy of 0.1 V at 800 mA g<sup>-1</sup>, with the output power reaching 0.17 and 0.19 mW cm<sup>-2</sup> in darkness and light, respectively (Fig. 5f), indicating an 11.8% surge in output power. These findings provide compelling evidence supporting the notion that light can stimulate charge transfer, augment redox activity, and expedite the charge-discharge process.

EIS measurements were carried out at the open-circuit potential of the PR-LIB using a constant potential mode with a voltage amplitude of 5 mV in the frequency range of 50 kHz to 1 Hz (Fig. 5g). The equivalent circuit model consists of the electrolyte resistance ( $R_e$ ), the electrode surface layer resistance ( $R_s$ ), the charge transfer resistance ( $R_{ct}$ ), and the Li<sup>+</sup> diffusion resistance ( $W$ ). The diameters of the circles reflect  $R_s$  and  $R_{ct}$ , which indicate the charge conductivity at the electrolyte/electrode interface. Lower  $R_s$  and  $R_{ct}$  values indicate more accessible charge transfer behavior at the interface [62]. Fig. 5h shows that light exhibits lower electrode surface layer resistance and charge transfer resistance than in the dark. Li<sup>+</sup> diffusion resistance was significantly reduced in light. These phenomena suggest that the accumulation of photogenerated carriers hastens the charge separation and transfer process. Simultaneously, we tested the PR-LIB impedance at 30°C (Fig. S8) and found that the Li<sup>+</sup> diffusion resistance was 55.31 Ω at 30°C, which is higher than under light illumination.

The electrochemical analyses demonstrate that the battery exhibits faster Li<sup>+</sup> diffusion, lower resistance, and higher capacity upon light excitation owing to accelerated reaction kinetics and

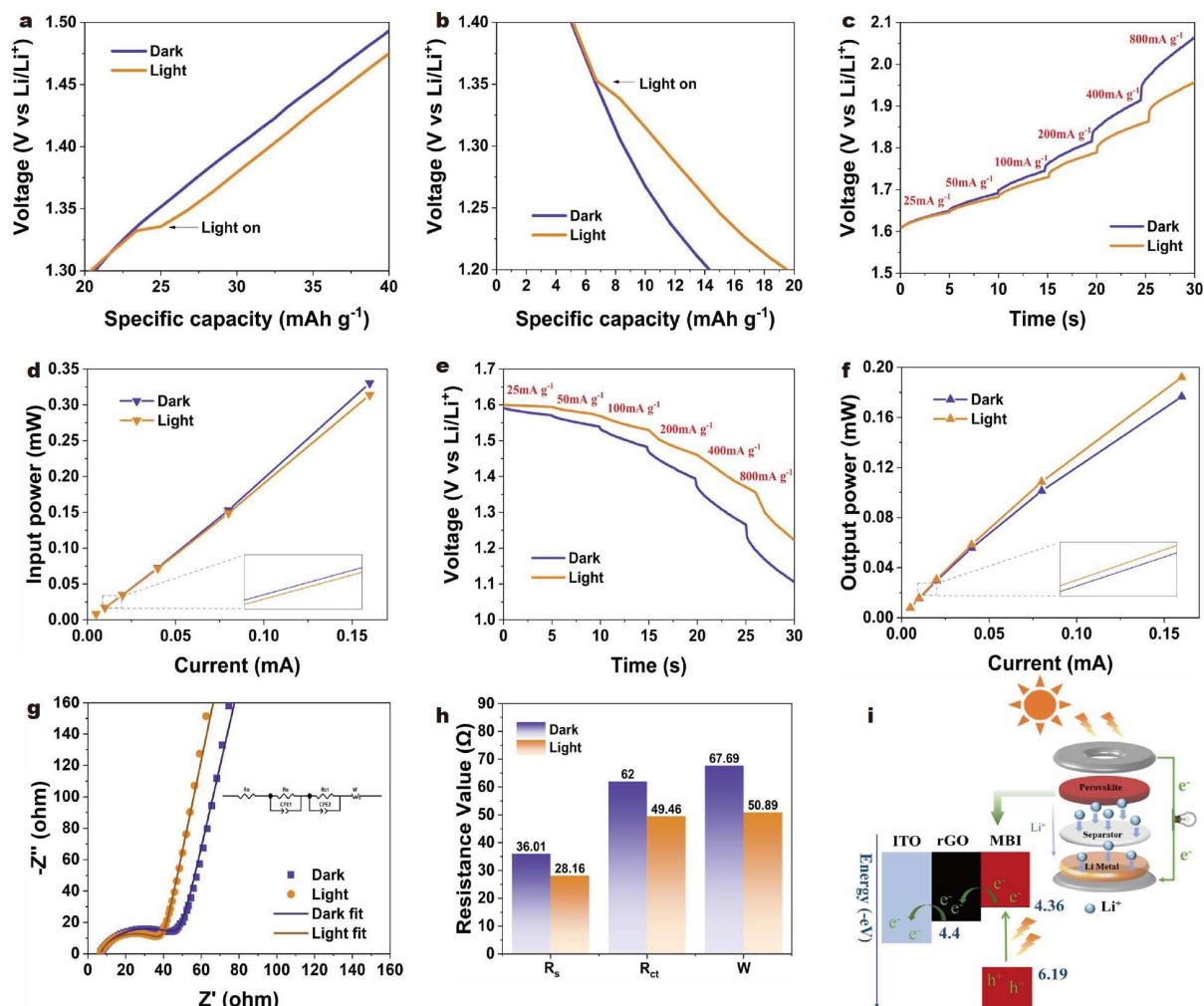


**Figure 5** (a) Galvanostatic charge curves at 50 mA g<sup>-1</sup> with sudden addition of light. (b) Galvanostatic discharge curves at 50 mA g<sup>-1</sup> with the sudden addition of light. (c)  $T$ - $V$  and (d)  $I$ - $P$  curves of PR-LIB during charging. (e)  $T$ - $V$  and (f)  $I$ - $P$  curves of PR-LIB during discharging. (g) Nyquist plots with and without light, where the inset shows the equivalent circuit. (h) Electrode surface layer resistance values, charge transfer resistance values, and Li<sup>+</sup> diffusion resistance values are compared under light and dark conditions. (i) The working mechanism of the PR-LIB based on MBI.

increased electron density. Therefore, light effectively enhances the electrochemical performance of PR-LIB. The PR-LIB working mechanism is as follows: During the charging and storage process, when the energy is equal to or greater than the bandgap, the material's surface generates photogenerated holes and repels the interlayer Li<sup>+</sup> into the electrolyte by electrostatic action. When light irradiates the MBI through the glass, photogenerated holes are produced by the material after absorbing energy. These holes move to the material's surface and repel Li<sup>+</sup> from the intercalation layer into the electrolyte through electrostatic action. The electrons generated by the light are transferred to the lithium sheet through the external circuit. Simultaneously, the Li<sup>+</sup> in the electrolyte moves towards the negative electrode and combines with the electrons, resulting in a chemical reaction that reduces the Li<sup>+</sup> to metallic lithium (Fig. 5i). The discharging process is the reverse of the charging process, and these two cycles are repeated to achieve energy conversion and storage.

## CONCLUSIONS

In this study, a novel methodology is recommended to enhance the functionality of the photo-rechargeable lithium-ion battery,

by utilizing non-hazardous, air-stable bismuth-based hybrid perovskite ((CH<sub>3</sub>NH<sub>3</sub>)<sub>3</sub>Bi<sub>2</sub>I<sub>6</sub>) as a photoelectric electrode. This substance possesses the dual functionality of transforming solar energy into electrical power and retaining it in the form of chemical energy. This investigation demonstrates from diverse angles that the efficacious charge separation of the photoelectric electrode promotes Li<sup>+</sup> transportation and enhances the efficiency of the cell. *ex-situ* XRD studies confirm that the lithium storage mechanism in MBI involves a blend of embedding and conversion procedures. Under illumination conditions, the discharge capacity of the cell increased from 236 mA h g<sup>-1</sup> in darkness to 282.4 mA h g<sup>-1</sup> at a current density of 50 mA g<sup>-1</sup>, an increase of 19.7%. The photogenerated carriers from the MBI effectively accelerated the charge transfer and lithium-ion diffusion, which contributed to the increase of the capacity and the decrease of the charge-transfer resistance. From an energy conservation perspective, light further enhanced the performance of the battery with a 0.1 V decrease in charging potential and a 6% reduction in input power, while a 0.1 V increase in discharge potential resulted in an 11.8% increase in output power. The findings of this study pave the path for the devel-

opment of next-generation energy storage systems that are not only more efficient but also environmentally friendly, rendering the proposed system an optimal candidate for energy harvesting and storage in portable devices.

Received 11 September 2024; accepted 20 December 2024;  
published online 28 February 2025

- Kabir E, Kumar P, Kumar S, *et al.* Solar energy: potential and future prospects. *Renew Sustain Energy Rev*, 2018, 82: 894–900
- Kruitwagen L, Story KT, Friedrich J, *et al.* A global inventory of photovoltaic solar energy generating units. *Nature*, 2021, 598: 604–610
- Mahmoud M, Ramadan M, Olabi AG, *et al.* A review of mechanical energy storage systems combined with wind and solar applications. *Energy Convers Manage*, 2020, 210: 112670
- Lv J, Xie J, Mohamed AGA, *et al.* Photoelectrochemical energy storage materials: design principles and functional devices towards direct solar to electrochemical energy storage. *Chem Soc Rev*, 2022, 51: 1511–1528
- Zeng Q, Lai Y, Jiang L, *et al.* Integrated photorechargeable energy storage system: next-generation power source driving the future. *Adv Energy Mater*, 2020, 10: 1903930
- Zha W, Ruan Q, Ma L, *et al.* Highly stable photo-assisted zinc-ion batteries via regulated photo-induced proton transfer. *Angew Chem Int Ed*, 2024, 63: e202400621
- Paoletta A, Vijn A, Guerfi A, *et al.* Review—Li-ion photo-batteries: challenges and opportunities. *J Electrochem Soc*, 2020, 167: 120545
- Yu X, Liu G, Wang T, *et al.* Recent advances in the research of photo-assisted lithium-based rechargeable batteries. *Chem Eur J*, 2022, 28: e202202104
- Salunke AD, Chamola S, Mathieson A, *et al.* Photo-rechargeable Li-ion batteries: device configurations, mechanisms, and materials. *ACS Appl Energy Mater*, 2022, 5: 7891–7912
- Liu Y, Li N, Wu S, *et al.* Reducing the charging voltage of a Li-O<sub>2</sub> battery to 1.9 V by incorporating a photocatalyst. *Energy Environ Sci*, 2015, 8: 2664–2667
- Liu YH, Qu J, Chang W, *et al.* A photo-assisted reversible lithium-sulfur battery. *Energy Storage Mater*, 2022, 50: 334–343
- Tan YX, Zhang X, Lin J, *et al.* A perspective on photoelectrochemical storage materials for coupled solar batteries. *Energy Environ Sci*, 2023, 16: 2432–2447
- Lee A, Vörös M, Dose WM, *et al.* Photo-accelerated fast charging of lithium-ion batteries. *Nat Commun*, 2019, 10: 4946
- Ren C, Zhou Q, Jiang W, *et al.* Investigation of germanium selenide electrodes for the integrated photo-rechargeable battery. *Int J Energy Res*, 2020, 44: 6015–6022
- Wilhelm M, Adam R, Bhardwaj A, *et al.* Carbon-coated electrospun V<sub>2</sub>O<sub>5</sub> nanofibers as photoresponsive cathode for lithium-ion batteries. *Adv Eng Mater*, 2023, 25: 2200765
- Kumar A, Thakur P, Sharma R, *et al.* Photo rechargeable Li-ion batteries using nanorod heterostructure electrodes. *Small*, 2021, 17: 2105029
- Tewari N, Shivarudraiah SB, Halpert JE. Photorechargeable lead-free perovskite lithium-ion batteries using hexagonal Cs<sub>3</sub>Bi<sub>2</sub>I<sub>9</sub> nanosheets. *Nano Lett*, 2021, 21: 5578–5585
- Lv J, Tan YX, Xie J, *et al.* Direct solar-to-electrochemical energy storage in a functionalized covalent organic framework. *Angew Chem Int Ed*, 2018, 57: 12716–12720
- Yang Z, Zhu P, Ullah Z, *et al.* Synchronous light harvesting and energy storing organic cathode material 1,4-dihydroxyanthraquinone for lithium-ion batteries. *Chem Eng J*, 2023, 468: 143787
- Qiang Y, Zhang L, Shao S, *et al.* Optoelectronic and photo-charging properties of CH<sub>3</sub>NH<sub>3</sub>PbI<sub>3</sub>/LiFePO<sub>4</sub> system. *Int J Energy Res*, 2021, 45: 6426–6435
- Ahmad S, George C, Beesley DJ, *et al.* Photo-rechargeable organo-halide perovskite batteries. *Nano Lett*, 2018, 18: 1856–1862
- Wang J, Wang Y, Zhu C, *et al.* Photoinduced rechargeable lithium-ion battery. *ACS Appl Mater Interfaces*, 2022, 14: 4071–4078
- Nguyen O, Courtin E, Sauvage F, *et al.* Shedding light on the light-driven lithium ion de-insertion reaction: towards the design of a photo-rechargeable battery. *J Mater Chem A*, 2017, 5: 5927–5933
- Andriamidamanana C, Sagaidak I, Bouteau G, *et al.* Light-induced charge separation in mixed electronic/ionic semiconductor driving lithium-ion transfer for photo-rechargeable electrode. *Adv Sustain Syst*, 2018, 2: 1700166
- Yan W, Wang J, Hu Q, *et al.* Approaching the theoretical capacity of TiO<sub>2</sub> anode in a photo-rechargeable lithium-ion battery. *Nano Res*, 2024, 17: 2655–2662
- Kato K, Puthirath AB, Mojiypour A, *et al.* Light-assisted rechargeable lithium batteries: organic molecules for simultaneous energy harvesting and storage. *Nano Lett*, 2021, 21: 907–913
- Chen Y, Chen Z, Zhang X, *et al.* An organic-halide perovskite-based photo-assisted Li-ion battery for photoelectrochemical storage. *Nanoscale*, 2022, 14: 10903–10909
- Liu S, Ding Z, Jiang T, *et al.* Photo-rechargeable lithium-ion batteries based on V<sub>2</sub>O<sub>5</sub> nanorods/TiO<sub>2</sub> heterostructure. *J Energy Storage*, 2024, 84: 110822
- Hu C, Chen L, Hu Y, *et al.* Light-motivated SnO<sub>2</sub>/TiO<sub>2</sub> heterojunctions enabling the breakthrough in energy density for lithium-ion batteries. *Adv Mater*, 2021, 33: 2103558
- Ciria-Ramos I, Juarez-Perez EJ, Haro M. Solar energy storage using a Cu<sub>2</sub>O-TiO<sub>2</sub> photocathode in a lithium battery. *Small*, 2023, 19: 2301244
- Boruah BD, Wen B, De Volder M. Light rechargeable lithium-ion batteries using V<sub>2</sub>O<sub>5</sub> cathodes. *Nano Lett*, 2021, 21: 3527–3532
- Gonzalez-Pedro V, Juarez-Perez EJ, Arsyad WS, *et al.* General working principles of CH<sub>3</sub>NH<sub>3</sub>PbX<sub>3</sub> perovskite solar cells. *Nano Lett*, 2014, 14: 888–893
- Wu Z, Sang S, Zheng J, *et al.* Crystallization kinetics of hybrid perovskite solar cells. *Angew Chem Int Ed*, 2024, 63: e202319170
- Zhang J, Tang S, Zhu M, *et al.* The role of grain boundaries in organic-inorganic hybrid perovskite solar cells and its current enhancement strategies: a review. *Energy & Environ Mater*, 2024, 7: e12696
- Luo M, Tarasov A, Zhang H, *et al.* Hybrid perovskites unlocking the development of light-emitting solar cells. *Nat Rev Mater*, 2024, 9: 295–297
- Zhang X, Liu H, Wang W, *et al.* Hybrid perovskite light-emitting diodes based on perovskite nanocrystals with organic-inorganic mixed cations. *Adv Mater*, 2017, 29: 1606405
- Liu P, He X, Ren J, *et al.* Organic-inorganic hybrid perovskite nanowire laser arrays. *ACS Nano*, 2017, 11: 5766–5773
- Lourenço SA, Figueredo LS, da Silva MAT, *et al.* Effect of incorporation of PbS nanocrystals on optical properties of the hybrid organic-inorganic MAPbI<sub>3</sub> perovskite. *Synth Met*, 2023, 297: 117400
- Zhang T, Hu C, Yang S. Ion migration: a “double-edged sword” for halide-perovskite-based electronic devices. *Small Methods*, 2020, 4: 1900552
- Walsh A, Stranks SD. Taking control of ion transport in halide perovskite solar cells. *ACS Energy Lett*, 2018, 3: 1983–1990
- Zhang L, Miao J, Li J, *et al.* Halide perovskite materials for energy storage applications. *Adv Funct Mater*, 2020, 30: 2003653
- Tewari N, Lam D, Li CHA, *et al.* Recent advancements in batteries and photo-batteries using metal halide perovskites. *APL Mater*, 2022, 10: 040905
- Mathieson A, Rahil M, Zhang Y, *et al.* Ruddlesden popper 2D perovskites as Li-ion battery electrodes. *Mater Adv*, 2021, 2: 3370–3377
- Vicente N, Garcia-Belmonte G. Methylammonium lead bromide perovskite battery anodes reversibly host high Li-ion concentrations. *J Phys Chem Lett*, 2017, 8: 1371–1374
- Xia HR, Sun WT, Peng LM. Hydrothermal synthesis of organometal halide perovskites for Li-ion batteries. *Chem Commun*, 2015, 51: 13787–13790
- Han B, Zhao J, Luo Z, *et al.* Energy storage research of metal halide perovskites for rechargeable batteries. *Nano Energy*, 2023, 115: 108646
- Zhang X, Jiao L, Wang Y. Molecular photoelectrochemical energy storage materials for coupled solar batteries. *Acc Chem Res*, 2024, 57: 1736–1746
- Ni C, Hedley G, Payne J, *et al.* Charge carrier localised in zero-

- dimensional  $(\text{CH}_3\text{NH}_3)_3\text{Bi}_2\text{I}_9$  clusters. *Nat Commun*, 2017, 8: 170
- 49 Lyu M, Yun JH, Cai M, *et al.* Organic-inorganic bismuth (III)-based material: a lead-free, air-stable and solution-processable light-absorber beyond organolead perovskites. *Nano Res*, 2016, 9: 692–702
- 50 Jakubas R, Zaleski J, Sobczyk L. Phase transitions in  $(\text{CH}_3\text{NH}_3)_3\text{Bi}_2\text{I}_9$  (MAIB). *Ferroelectrics*, 1990, 108: 109–114
- 51 Abulikemu M, Ould-Chikh S, Miao X, *et al.* Optoelectronic and photovoltaic properties of the air-stable organohalide semiconductor  $(\text{CH}_3\text{NH}_3)_3\text{Bi}_2\text{I}_9$ . *J Mater Chem A*, 2016, 4: 12504–12515
- 52 Kong M, Hu H, Wan L, *et al.* Nontoxic  $(\text{CH}_3\text{NH}_3)_3\text{Bi}_2\text{I}_9$  perovskite solar cells free of hole conductors with an alternative architectural design and a solution-processable approach. *RSC Adv*, 2017, 7: 35549–35557
- 53 Park BW, Philippe B, Zhang X, *et al.* Bismuth based hybrid perovskites  $\text{A}_3\text{Bi}_2\text{I}_9$  (A: methylammonium or cesium) for solar cell application. *Adv Mater*, 2015, 27: 6806–6813
- 54 Fabian DM, Ardo S. Hybrid organic-inorganic solar cells based on bismuth iodide and 1,6-hexanediammonium dication. *J Mater Chem A*, 2016, 4: 6837–6841
- 55 Roy K, Li T, Ogale S, *et al.* Hybrid perovskite-like iodobismuthates as low-cost and stable anode materials for lithium-ion battery applications. *J Mater Chem A*, 2021, 9: 2689–2693
- 56 Hao B, Yan Y, Wang X, *et al.* Synthesis of anatase  $\text{TiO}_2$  nanosheets with enhanced pseudocapacitive contribution for fast lithium storage. *ACS Appl Mater Interfaces*, 2013, 5: 6285–6291
- 57 Liu S, Zhang K, Tan L, *et al.* All-inorganic halide perovskite  $\text{CsPbBr}_3$ @CNTs composite enabling superior lithium storage performance with pseudocapacitive contribution. *Electrochim Acta*, 2021, 367: 137352
- 58 Vicente N, Garcia-Belmonte G. Organohalide perovskites are fast ionic conductors. *Adv Energy Mater*, 2017, 7: 1700710
- 59 Dawson JA, Naylor AJ, Eames C, *et al.* Mechanisms of lithium intercalation and conversion processes in organic-inorganic halide perovskites. *ACS Energy Lett*, 2017, 2: 1818–1824
- 60 Pujari A, Kim BM, Sayed FN, *et al.* Does heat play a role in the observed behavior of aqueous photobatteries? *ACS Energy Lett*, 2023, 8: 4625–4633
- 61 Dong Q, Wei M, Zhang Q, *et al.* Photoassisted Li-ion de-intercalation and  $\text{Ni}^{2+}$  valence conversion win-win boost energy storage performance in  $\text{Ni}/\text{CdS}/\text{Ni}_3\text{S}_2$ -based Li-ion battery. *Chem Eng J*, 2023, 459: 141542
- 62 Fujii Y, Ramirez D, Rosero-Navarro NC, *et al.* Two-dimensional hybrid halide perovskite as electrode materials for all-solid-state lithium secondary batteries based on sulfide solid electrolytes. *ACS Appl Energy Mater*, 2019, 2: 6569–6576

**Acknowledgement** This work was supported by the National Key R&D Program of China (2020YFA0710404 and 2022YFB4200301), the National Natural Science Foundation of China (52232008, 51972110, 52102245, 52072121, 52402254, 22109002 and 22409061), the Beijing Natural Science Foundation (2222076, 2222077 and Z240024), the Beijing Nova Program (20220484016), the Young Elite Scientists Sponsorship Program by CAST (2022QNRC001), the 2022 Strategic Research Key Project of Science and Technology Commission of the Ministry of Education, the Huaneng Group Headquarters Science and Technology Project (HNKJ20-H88), the State Key Laboratory of Alternate Electrical Power System with Renewable Energy Sources (LAPS2024-05), the Fundamental Research Funds for the Central Universities (2022MS029, 2022MS02, 2022MS031, 2023MS042, 2023MS047, 2023MS042 and 2023MS047) and the NCEPU “Double First-Class” Program.

**Author contributions** Yin X designed and performed the experiments, analyzed the data, and wrote the manuscript. Di G and Sun X helped to analyze the data. Liu Y, Wang G, Mi C, Kuang Y and Xiang X helped to perform the experiment, and gave some advice for the data analysis. Eran Edri helped to analysis the data and polish the language. Lv X and Li M conceived the project, reviewed and supervised the manuscript. All authors discussed the results and reviewed the manuscript.

**Conflict of interest** The authors declare that they have no conflict of interest.

**Supplementary information** Supplementary materials are available in the online version of the paper.



**Xiaojun Lv** is a Professor at the School of New Energy, North China Electric Power University. His research focuses on solar energy conversion and storage, hydrogen energy, and photo-rechargeable devices.



**Meicheng Li** is a Professor at North China Electric Power University and serves as the Dean of the School of New Energy. His primary focus is on the research of new energy technologies, such as perovskite solar cells, lithium-ion batteries, and photo-rechargeable devices.



**Xiaojing Yin** is currently a graduate student at North China Electric Power University (NCEPU), and completed her undergraduate studies at the School of New Energy at NCEPU. Her research interests focus on the design and performance research of photo-rechargeable devices.

## 一种基于无铅杂化钙钛矿的光充电锂离子电池: 实现节能与高性能储能双突破

殷小净<sup>1</sup>, 邱广然<sup>1</sup>, 刘晔<sup>1</sup>, 王国强<sup>1</sup>, 米倡华<sup>1</sup>, 匡宇博<sup>1</sup>, 向小倩<sup>1</sup>, 孙鑫<sup>1</sup>, Eran Edri<sup>2</sup>, 吕小军<sup>1\*</sup>, 李美成<sup>1\*</sup>

**摘要** 清洁能源的开发和高效利用已成为推动当代社会可持续发展的核心技术之一。在这一背景下, 光充电锂离子电池(Photo-Rechargeable Lithium-Ion Batteries, PR-LIB)因其能够同时解决太阳能间歇性问题和实现电池自充电的特性, 受到了广泛关注。本研究设计并制备了一种基于无铅铋基杂化钙钛矿( $(\text{CH}_3\text{NH}_3)_3\text{Bi}_2\text{I}_9$ )的光活性电极, 该电极不仅具备高效的光电转换能力, 还能够将太阳能以化学能的形式储存于电池内部, 从而实现光能与电能的双重利用。实验结果表明, 在光照条件下, 基于该电极的PR-LIB放电容量从黑暗中的 $236 \text{ mAh g}^{-1}$ 显著提升至 $282.4 \text{ mAh g}^{-1}$  (电流密度为 $50 \text{ mA g}^{-1}$ )。容量增长率达到19.7%。这一性能提升主要归因于铋基杂化钙钛矿材料在光照下产生的光生载流子, 这些载流子有效促进了电极内部的电荷转移过程, 并加速了锂离子的扩散动力学, 从而显著降低了电荷转移电阻并提高了电池的整体效率。此外, 在光照条件下, 电池的充电电位降低了0.1 V (对应输入功率减少6%), 而放电电压则升高了0.1 V (对应输出功率增加11.8%)。本研究不仅揭示了铋基杂化钙钛矿在光充电电池中的独特优势, 还为下一代高效、节能、环境友好的储能系统提供了新的设计思路, 尤其是在便携式电子设备领域展现了广阔的应用前景。